ELSEVIER

Journal of Fluids and Structures 23 (2007) 1–21

JOURNAL OF FLUIDS AND STRUCTURES

www.elsevier.com/locate/jfs

Excitation, inertia, and drag forces on a cylinder vibrating transversely to a steady flow

L. Kaiktsis[a,*], G.S. Triantafyllou[a], M. Özbas[b]

[a]*Department of Naval Architecture and Marine Engineering, National Technical University of Athens, P.O. Box 64033, Zografos 15710, Athens, Greece*

[b]*Department of Mechanical and Process Engineering, Swiss Federal Institute of Technology Zurich, Sonneggstrasse 3, CH-8092 Zürich, Switzerland*

Received 21 September 2004; accepted 6 August 2006
Available online 18 September 2006

Abstract

We present a computational study of the forces on a cylinder oscillating harmonically in the direction perpendicular to a uniform flow. The two-dimensional Navier–Stokes equations are solved on a coordinate system fixed on the cylinder. The Reynolds number is equal to 400. Several oscillation frequencies are considered: (a) resonant forcing, (b) forcing at frequency below the natural frequency of the wake, and (c) forcing at frequency above the natural frequency of the wake. Once the flow has reached a statistical steady state, the lift and drag forces on the cylinder are computed. The lift force in particular is decomposed into one component that is in phase with the velocity (excitation force), and one component that is 180° out of phase with the acceleration (inertia or added mass force). The variation of the forces as a function of the amplitude-over-diameter-ratio is studied in detail. It is found that the scaling of the so-called inertia component of the force with the acceleration of the cylinder can lead to serious problems at small amplitudes of oscillation, and that it is overall preferable to scale both components of the force with the dynamic pressure of the fluid. Through extensive flow visualization, it is shown that changes in the state of the flow are related to the abrupt changes of the forces with the amplitude-over-diameter-ratio. Moreover, qualitative differences are found between the results for the below resonance and the resonant or above resonance forcing. The former are characterized by smooth variation of the hydrodynamic force coefficients and spatially ordered vortex streets. The latter are characterized by continuous and sharp, even jump-like, changes of the forces, and a variety of vortex patterns in the wake, resulting for some combinations of frequency and amplitude of oscillation to spatially disordered vortex streets.

Keywords: Vortex-induced vibrations; Oscillating cylinder; Spectral element method

1. Introduction

The flow in the wake of a vibrating cylinder is a system with very rich physics that depends strongly on the frequency and amplitude of the oscillation. This flow has been the subject of many papers, far too many to cite here [see review articles by Sarpkaya (2004), Bearman (1984) and Williamson and Govardhan (2004)]. Moreover, measured forces on

*Corresponding author. Tel.: +30 210 7723386; fax: +30 210 7721117.
E-mail address: kaiktsis@naval.ntua.gr (L. Kaiktsis).

0889-9746/$ - see front matter © 2006 Elsevier Ltd. All rights reserved.
doi:10.1016/j.jfluidstructs.2006.08.006

cylinders forced to vibrate harmonically can be used to calculate the monochromatic response of flexible structures to vortex-induced vibrations.

Despite the large volume of such experimental data, a systematic investigation that relates the variation of the hydrodynamic forces to the flow patterns in the wake is missing. Numerical investigation of the flow past an oscillating cylinder at low Reynolds number has been done by, among others, Blackburn and Henderson (1999), Anagnostopoulos (2000), Baek et al. (2001), Blackburn et al. (2001) and Guilmineau and Queutey (2002), but for a very limited number of frequencies and amplitudes of oscillation, not sufficient to offer a picture of the dependence of the forces on these parameters.

In this paper we investigate the forces on a vibrating cylinder through time-dependent simulation of the Navier–Stokes equations. Several frequencies near the natural frequency of the wake are considered, and for each the force coefficients are calculated as a function of the amplitude-over-diameter-ratio. Amplitude-over-diameter-ratios for which energy is transferred from the fluid to the cylinder are of interest, since only those correspond to potential vortex-induced vibrations. Two-dimensional flow is considered for expediency. Here, we try to find a relation between the forces on the cylinder and the vortex patterns in the wake. The relevance of our results to real situations is limited by the low value of the Reynolds number and the two-dimensionality of the flow. We do expect, however, that some basic conclusions will be useful to higher Reynolds number too, and that the present detailed study can serve as a guide and reference point to the much more computationally expensive three-dimensional simulations.

2. Formulation and numerical method

We consider uniform flow past an oscillating cylinder. The velocity of the fluid far upstream of the cylinder is U_∞, the density and kinematic viscosity of the fluid are, respectively, ρ and ν. The coordinate axes are x, parallel to the flow, and y, normal to the flow. The cylinder has diameter D and is oscillating transversely to the flow with amplitude A and circular frequency ω. The instantaneous displacement of the cylinder η from its mean position is given by

$$\eta = A\sin(\omega t). \tag{1}$$

Let F_y be the lift force on the cylinder (per cylinder unit length), resulting from the integration of the pressure and viscous stresses around the cylinder. For a locked-in wake, F_y is also harmonic with the same frequency, and can be decomposed into the excitation force and the inertia or added mass force:

$$F_y = F_v\cos(\omega t) + F_M\sin(\omega t), \tag{2}$$

where F_v, F_M are the amplitudes of the excitation and added mass forces, respectively. If the force is harmonic, F_v, F_M can be calculated from F_y using the following relations:

$$F_v + \mathrm{i}F_M = \frac{2}{T}\int_0^T F_y\exp(\mathrm{i}\omega t)\,\mathrm{d}t, \tag{3}$$

where $\mathrm{i} = \sqrt{-1}$, and $T = 2\pi/\omega$ is the period of the cylinder oscillation.

It is customary to scale F_v, F_M as follows:

$$F_v = \tfrac{1}{2}\rho U_\infty^2 D C_{Lv}, \tag{4}$$

$$F_M = \frac{\pi}{4}\rho D^2 A\omega^2 C_M, \tag{5}$$

where C_{Lv} and C_M are nondimensional parameters. It is assumed, in other words, that F_v is proportional to the dynamic pressure $\frac{1}{2}\rho U_\infty^2$, and that F_M is proportional to the acceleration of the cylinder. This decomposition is not consistent however, since F_v and F_M are components of the same force. We will therefore consider scaling F_M with the dynamic pressure also, i.e.

$$F_M = \tfrac{1}{2}\rho U_\infty^2 D C_{La}, \tag{6}$$

where C_{La} is another nondimensional parameter. It is straightforward to show that $C_{La} = 2\pi^3(A/D)(D/U_\infty T)^2 C_M$, where T is the cylinder oscillation period.

When F_v and F_M are scaled based on the dynamic pressure, it is reasonable to also scale the whole lift force F_y the same way, i.e. to set

$$F_y = \tfrac{1}{2}\rho U_\infty^2 D C_L, \tag{7}$$

where C_L is the nondimensional transverse force (lift coefficient), which is a function of time, and can be decomposed into the time-averaged value $\langle C_L \rangle$ and the instantaneous fluctuation C'_L.

We can use the root mean square (r.m.s.) of C'_L, which we will denote by $C_{L,\mathrm{r.m.s.}}$, to characterize the fluctuations of the lift force. When the force on the cylinder is harmonic in time, it is straightforward to see that

$$C_{L,\mathrm{r.m.s.}} = \frac{1}{\sqrt{2}} \sqrt{C_{Lv}^2 + C_{La}^2}. \tag{8}$$

From dimensional analysis it follows that C_{Lv}, C_M, C_{La}, and C_L are all functions of the reduced amplitude $\xi = A/D$, of the nondimensional excitation frequency $f_e = \omega D/(2\pi U_\infty)$, and of the Reynolds number.

Also, let F_x denote the drag force on the cylinder, per cylinder unit length; the drag coefficient C_D is defined from the relation:

$$F_x = \tfrac{1}{2} \rho U_\infty^2 D C_D. \tag{9}$$

The drag coefficient can be decomposed into its time-averaged component $\langle C_D \rangle$ and its fluctuating component C'_D:

$$C_D = \langle C_D \rangle + C'_D, \tag{10}$$

where

$$\langle C_D \rangle = \frac{1}{T} \int_0^T C_D \, \mathrm{d}t. \tag{11}$$

We will denote the r.m.s. of C'_D by $C_{D,\mathrm{r.m.s}}$.

The main goals of this paper are to study, through numerical simulation, the variation of these hydrodynamic coefficients with the nondimensional oscillation amplitude and frequency, to relate the results to the wake structure, and to test the scaling assumptions made for the forces.

One additional parameter that is of interest is the mean power dissipation in the flow. Since the flows that we are considering have reached a statistical steady state, the mean power dissipation gives a quantitative indication of how energetic the flow is (the more energetic the flow, the higher the mean dissipation rate). If we denote by $\langle P_d \rangle$ the mean power dissipation, application of the fist law of thermodynamics gives the following expression for $\langle P_d \rangle$:

$$\langle P_d \rangle = \langle F_x \rangle U_\infty - \left\langle F_y \frac{\mathrm{d}\eta}{\mathrm{d}t} \right\rangle, \tag{12}$$

where $\mathrm{d}\eta/\mathrm{d}t$ is the lateral velocity of the cylinder. By dividing by $\frac{1}{2}\rho D U_\infty^3$ and using Eqs. (9), (11), (2), (1) and (4), we obtain

$$\langle P \rangle = \langle C_D \rangle - \pi C_{Lv} \left(\frac{A}{D} \right) f_e, \tag{13}$$

where $\langle P \rangle = \langle P_d \rangle / (\frac{1}{2}\rho D U_\infty^3)$ is the nondimensional mean power dissipation, and f_e is the nondimensional oscillation frequency of the cylinder.

The governing equations are the Navier–Stokes and incompressibility equations. For convenience, we have nondimensionalized all lengths with respect to D, all velocities with respect to the free stream velocity U_∞, time with respect to D/U_∞, and pressure with respect to ρU_∞^2. Then the incompressibility and Navier–Stokes read:

$$\nabla \cdot \vec{u} = 0, \tag{14}$$

$$\frac{\partial \vec{u}}{\partial t} + \vec{u} \cdot \nabla \vec{u} = -\nabla p + \frac{1}{R} \nabla^2 \vec{u}, \tag{15}$$

where $R = U_\infty D/\nu$ is the Reynolds number of the flow. Throughout the paper $R = 400$, a value very close to that in the experiments of Williamson and Roshko (1988).

The boundary conditions for the flow are as follows. (i) On the instantaneous position of the cylinder the velocity of the fluid is equal to that of the cylinder, i.e.

$$\vec{u} = \frac{\mathrm{d}\eta}{\mathrm{d}t} \vec{j}, \tag{16}$$

where η is now the nondimensional cylinder displacement, and $\vec{j}$ is the unit vector in the y direction. (ii) Far upstream and at the sides of the domain we have uniform flow, i.e. $\vec{u} = 1\vec{i}$ where $\vec{i}$ is the unit vector in the x direction (the dimensional velocity is equal to U_∞). (iii) Finally, far downstream we assume a Neumann condition for the velocity, $\partial \vec{u}/\partial n = 0$.

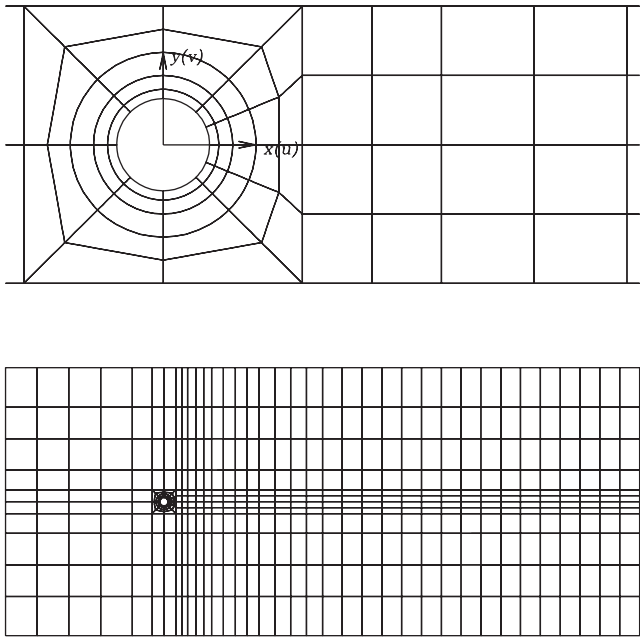

Fig. 1. Spectral element skeleton for flow around a circular cylinder, including elements close to the cylinder, and the entire mesh.

In order to avoid reconstructing the computational grid at each time step, we use coordinates that are fixed on the cylinder. With $\vec{u}$ now representing the relative, with respect to the moving cylinder, velocity, Eq. (14) remains unchanged, while, as is well known, (15) becomes

$$\frac{\partial \vec{u}}{\partial t} + \vec{u} \cdot \nabla \vec{u} = -\nabla p + \frac{1}{R} \nabla^2 \vec{u} - \frac{\mathrm{d}^2 \eta}{\mathrm{d}t^2} \vec{j}, \tag{17}$$

i.e. we have the appearance of a d'Alambert acceleration at the right-hand side. This of course means that, in order to find the actual force on the cylinder, one has to subtract from the computed force a "dynamic Archimedes" force equal to $-(\pi/4)\rho D^2 \, \mathrm{d}^2\eta/\mathrm{d}t^2 \vec{j}$.

Moreover, the boundary condition on the cylinder is reduced to $\vec{u} = 0$, while at the inflow and lateral boundaries we have $\vec{u} = 1\vec{i} - \mathrm{d}\eta/\mathrm{d}t\vec{j}$, whereas the Neumann condition is maintained at the outflow boundary.

Eqs. (14), (17) subject to the new boundary conditions are solved using a Legendre spectral element method, e.g. see Karniadakis (1989), with the time discretization based on a second-order accurate mixed stiffly stable scheme (Karniadakis et al., 1991). We have implemented the same numerical methodology in a number of previous investigations, e.g. see Delaunay and Kaiktsis (2001), Kaiktsis and Monkewitz (2003). The spectral element skeleton used is shown in Fig. 1. The inflow boundary is located at $x/D = -20$, the lateral boundaries at $y/D = \pm 17$, while the outflow boundary is at $x/D = 60$. We have implemented a discretization consisting of 464 macro-elements, with 9×9 elemental resolution. Typically, the values of the numerical time step were of the order of 0.0015 or lower. In selecting domain size and resolution parameters, we have been guided by previous numerical studies; see Evangelinos and Karniadakis (1999), Blackburn and Henderson (1999). Resolution tests, illustrating the adequacy of the present discretization, are presented in Appendix A.

3. Results

We present detailed results for the following five values of the reduced oscillation frequency $F = f_e/f_s$ (where f_s is the Strouhal number, i.e. the nondimensional vortex shedding frequency of flow past a stationary cylinder): (i) $f_e/f_s = 1$ (resonant forcing), (ii) $f_e/f_s = 0.9$, (iii) $f_e/f_s = 0.8$, (iv) $f_e/f_s = 1.1$, (v) $f_e/f_s = 1.2$. Note that here $f_s = 0.22017$, a value obtained from our two-dimensional simulations. [It is should be mentioned here that decreasing the reduced frequency F corresponds to increasing the wavelength parameter λ/D of the Williamson–Roshko map, see Fig. 3(a) in Williamson and Roshko (1988).] We have considered therefore resonant forcing, two cases of below resonance forcing,

and two cases of above resonance forcing. For each frequency of oscillation, we perform a detailed study, first of the variation of the hydrodynamic force coefficients with the value of the amplitude-over-diameter-ratio A/D, and then of the variation of the vortex patterns in the wake with A/D.

3.1. Variation of the hydrodynamic force coefficients

For each combination of A/D, F, the flow is computed until a statistical steady state is reached. Then the force in the y direction (lift force) is computed, and is decomposed into the excitation and inertia force. The excitation force is always scaled with the dynamic pressure, while for the inertia force we examine scaling both with the acceleration of the structure and with the dynamic pressure. The force in the x direction (drag force) is also computed, and is decomposed into its mean and fluctuating part.

3.1.1. Resonant forcing

We consider first the case where the excitation frequency is equal to the natural frequency of vortex shedding (resonant forcing). Then the flow is locked on to the excitation frequency for any amplitude of oscillation. The variation of the coefficients C_{Lv}, C_M, C_{La}, $C_{L,\mathrm{r.m.s.}}$, and the time-averaged and r.m.s. fluctuation values of the drag coefficient, $\langle C_D \rangle$ and $C_{D,\mathrm{r.m.s.}}$, with respect to A/D, are shown in Figs. 2–7. We observe that C_{Lv} is initially rather insensitive to A/D, and then starts to decrease.

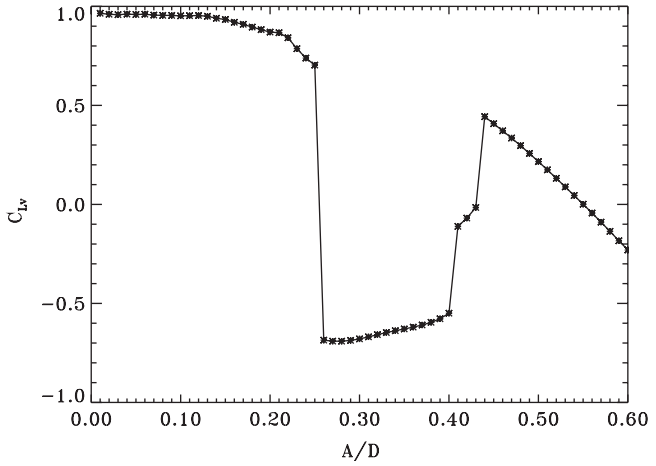

Fig. 2. Excitation force coefficient C_{Lv}, versus nondimensional excitation amplitude, for $F = 1.0$.

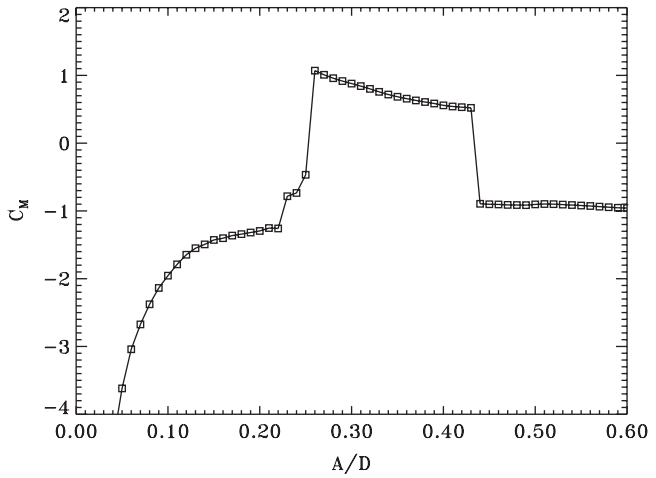

Fig. 3. Inertia force coefficient C_M, versus nondimensional excitation amplitude, for $F = 1.0$.

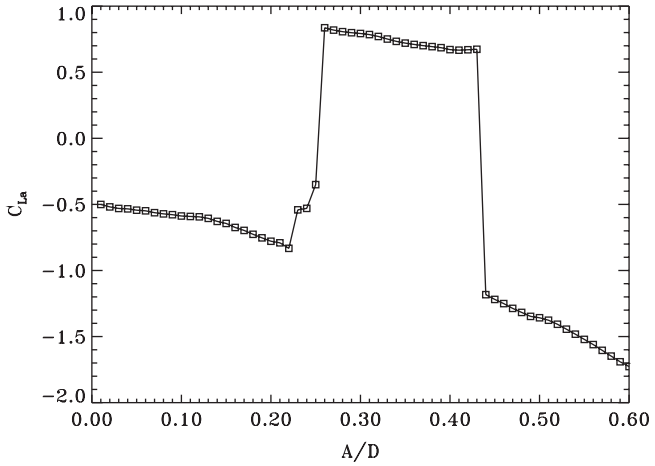

Fig. 4. Inertia force coefficient C_{La}, versus nondimensional excitation amplitude, for $F = 1.0$.

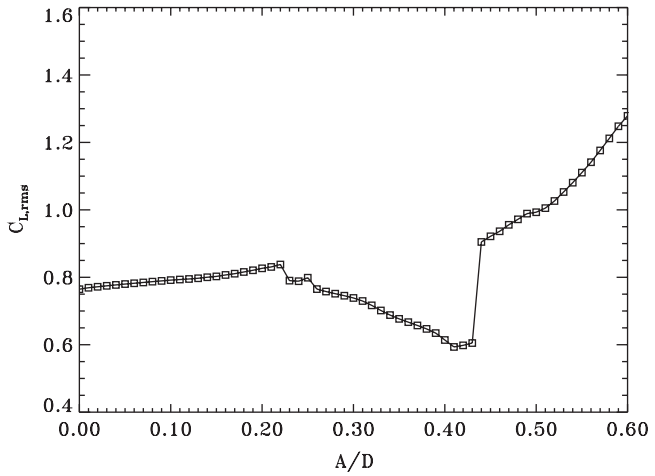

Fig. 5. R.m.s. fluctuation intensity of lift coefficient versus nondimensional excitation amplitude, for $F = 1.0$.

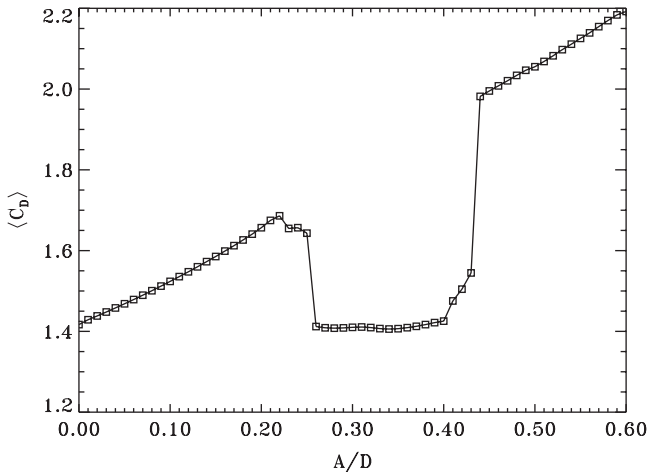

Fig. 6. Time-averaged drag coefficient versus nondimensional excitation amplitude, for $F = 1.0$.

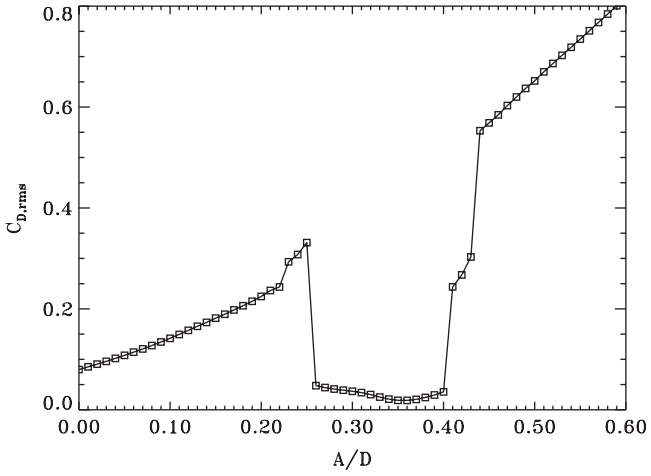

Fig. 7. R.m.s. fluctuation intensity of drag coefficient versus nondimensional excitation amplitude, for $F = 1.0$.

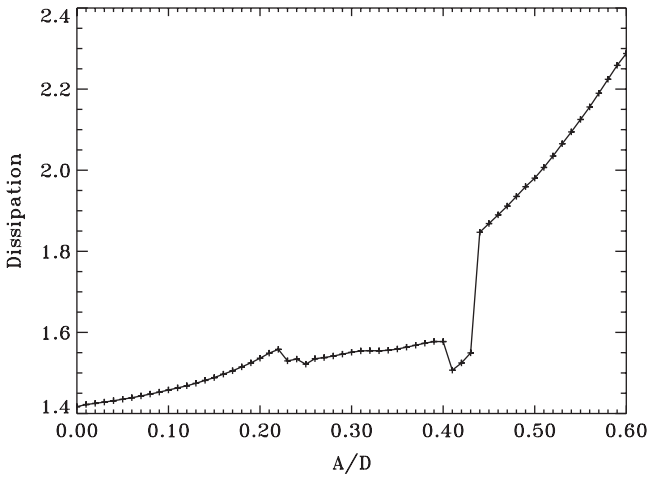

Fig. 8. Time-averaged nondimensional power dissipation versus nondimensional excitation amplitude, for $F = 1.0$.

For $A/D = 0.26$, however, C_{Lv} abruptly falls to negative values, indicating that energy flows from the cylinder to the flow, i.e. that the fluid force acts like damping on the structure. The value of C_{Lv} remains negative as A/D is increased, until, for $A/D = 0.42$, a new jump is observed, this time towards positive values. Then C_{Lv} smoothly decreases and vanishes at about $A/D = 0.55$. In fact, this part of the curve seems like a continuation of the initial part of the curve, suggesting that the abrupt changes correspond to transitions between two different modes of vortex shedding.

After the first transition, the average and fluctuating part of the drag coefficient are also reduced (see Figs. 6 and 7). The second transition is accompanied by a sudden increase in the mean and fluctuating drag components. We have calculated the nondimensional mean power dissipation in the flow as a function of A/D (Fig. 8). The dissipation seems to level off after the sudden drop in the mean drag coefficient, indicating a less energetic flow with reduced fluctuations of velocity and pressure. After the second abrupt change of the forces, the mean dissipation increases rapidly with A/D again. Overall, the mean dissipation varies with A/D much more smoothly than the hydrodynamic force coefficients.

In the region of reduced drag, the added mass coefficient C_M is fairly close to one (Fig. 3). Conversely, for small values of A/D, C_M obtains high negative values and it appears to tend to minus infinity when $A/D \to 0$. This is due to the fact that, for small values of A/D, there is a finite force in phase with the acceleration, whose amplitude is nearly constant, and not proportional to the acceleration of the cylinder. The singular behavior can be eliminated readily if we simply re-scale F_M in Eq. (5) with the dynamic pressure (see Eq. (6) and the corresponding results in Fig. 4).

3.1.2. Forcing at below the natural frequency

We next consider forcing at below the resonant frequency. Two different cases are considered; in the first, the frequency of oscillation is equal to 0.9 times the natural frequency of vortex shedding, and in the second case equal to 0.8 times the natural frequency of vortex shedding. The variations of C_{Lv}, C_M, C_{La}, $C_{L,\mathrm{r.m.s.}}$, C_D, and $C_{D,\mathrm{r.m.s.}}$ for both frequencies are shown in Figs. 9–14. In these graphs, the results of the resonant forcing are also included for easy comparisons.

For non-resonant forcing, for small amplitudes of oscillation, the vortex shedding is not locked on to the excitation frequency. Lock-in occurs for A/D larger than about 0.1 for $f_e/f_s = 0.9$, and for A/D larger than about 0.2 for $f_e/f_s = 0.8$. (We infer therefore that the boundary of the lock-in region in the f_e/f_s versus A/D plane is nearly a straight line with slope equal to one.) The onset of lock-in has a very visible effect on all hydrodynamic coefficients through the fact that the slope of all curves becomes discontinuous there. The variation of all force coefficients with A/D remains otherwise smooth without any type of discontinuities.

For $F = 0.9$, the coefficient C_{Lv} starts increasing after lock-in has been established, and, after reaching a maximum, decays and eventually becomes negative (see Fig. 9). Unlike the resonant case, however, the variation is smooth without

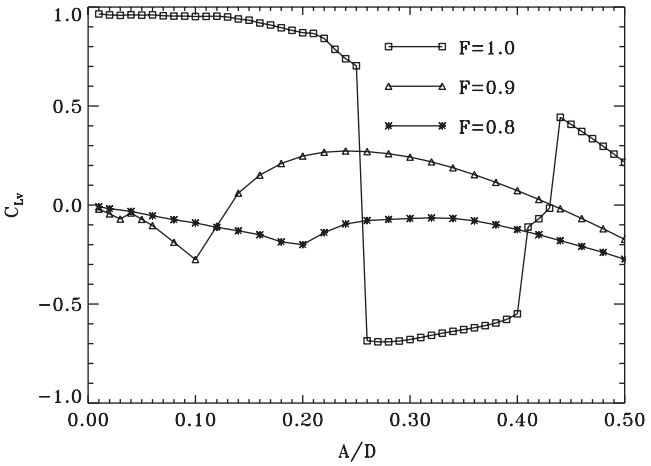

Fig. 9. Excitation force coefficient C_{Lv}, versus nondimensional excitation amplitude, for different values of reduced excitation frequency ($F \leqslant 1$).

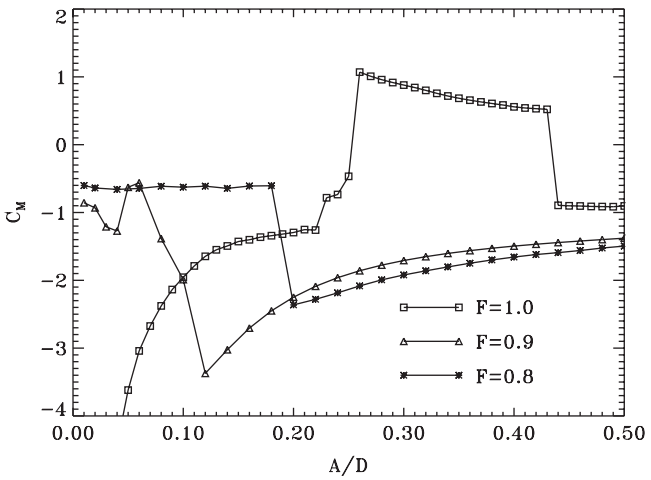

Fig. 10. Inertia force coefficient C_M, versus nondimensional excitation amplitude, for different values of reduced excitation frequency ($F \leqslant 1$).

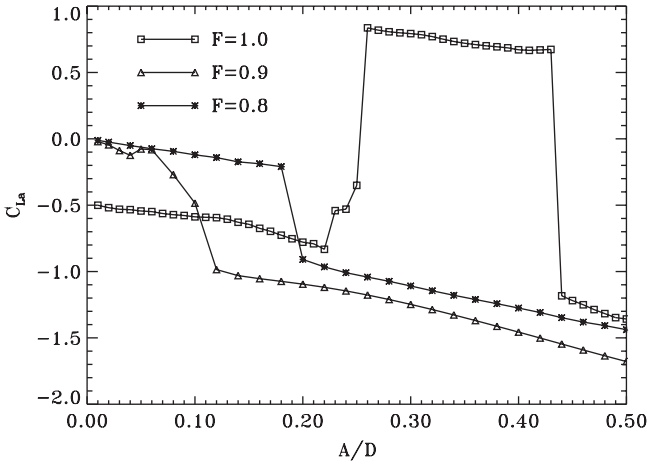

Fig. 11. Inertia force coefficient C_{La}, versus nondimensional excitation amplitude, for different values of reduced excitation frequency ($F \leqslant 1$).

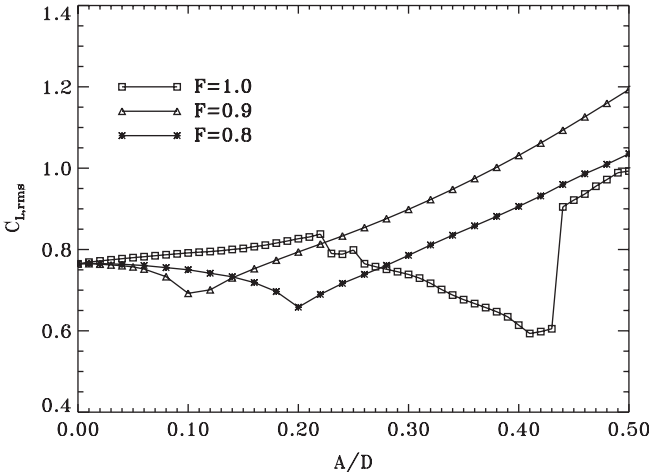

Fig. 12. R.m.s. fluctuation intensity of lift coefficient versus nondimensional excitation amplitude, for different values of reduced excitation frequency ($F \leqslant 1$).

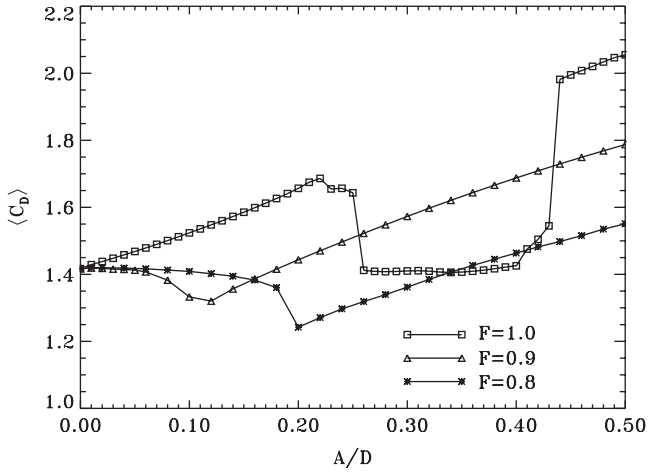

Fig. 13. Time-averaged drag coefficient versus nondimensional excitation amplitude, for different values of reduced excitation frequency ($F \leqslant 1$).

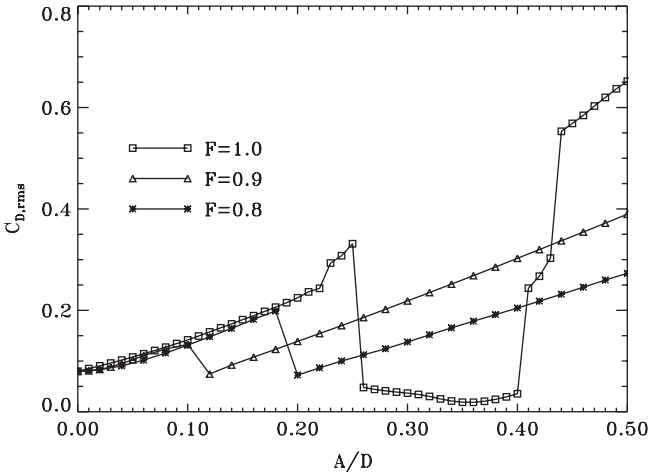

Fig. 14. R.m.s. fluctuation intensity of drag coefficient versus nondimensional excitation amplitude, for different values of reduced excitation frequency ($F \leqslant 1$).

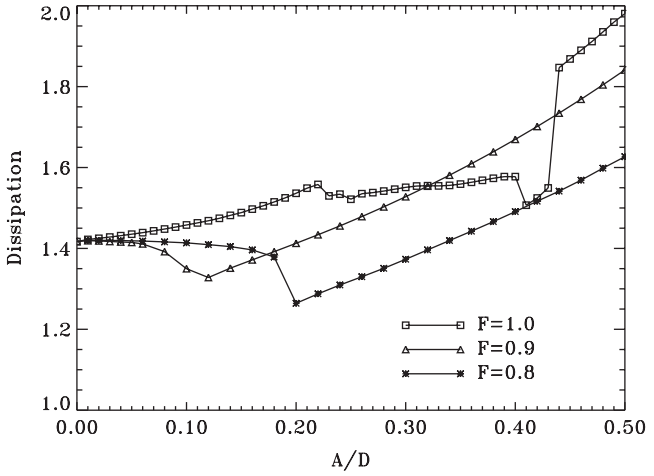

Fig. 15. Time-averaged nondimensional power dissipation versus nondimensional excitation amplitude, for different values of reduced excitation frequency ($F \leqslant 1$).

the sudden drop that is present in the case of resonant forcing. The decay of C_{Lv} appears to be almost linear with A/D. We note that this overall variation of C_{Lv}, i.e. initially negative, then positive and finally negative again, is in qualitative agreement to what has been reported in experiments at high Reynolds numbers, see Gopalkrishnan (1993).

In Fig. 10 we observe that the added mass coefficient C_M remains negative for all values of A/D, suggesting that the term "added mass" or "inertia" force is not really the most appropriate, since the corresponding component of the force is not 180 degrees out of phase with the accelaration. The coefficient C_M does not exhibit the divergence at zero A/D that the resonant case exhibits. Still, for low amplitudes, scaling the inertia force with the dynamic pressure (Fig. 11) gives more meaningful values for the nondimensional coefficient C_{La}, and seems overall preferable.

For below resonant forcing, the average drag coefficient increases monotonically with A/D after lock-in (Fig. 13). The drag fluctuations are increasing functions of A/D, with a drop at lock-in (Fig. 14). The mean power dissipation in the flow (Fig. 15) also does not exhibit dramatic changes, and keeps increasing with the A/D ratio after lock-in, suggesting that the vortex patterns in the wake remain qualitatively the same for all values of A/D. This is confirmed by computer visualizations (see below).

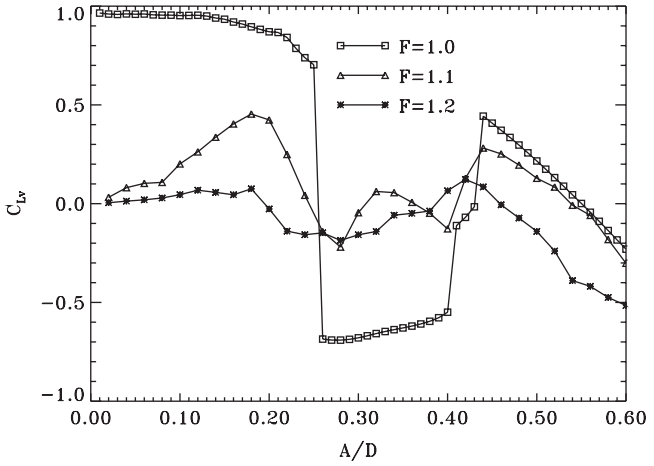

Fig. 16. Excitation force coefficient C_{Lv}, versus nondimensional excitation amplitude, for different values of reduced excitation frequency ($F \geqslant 1$).

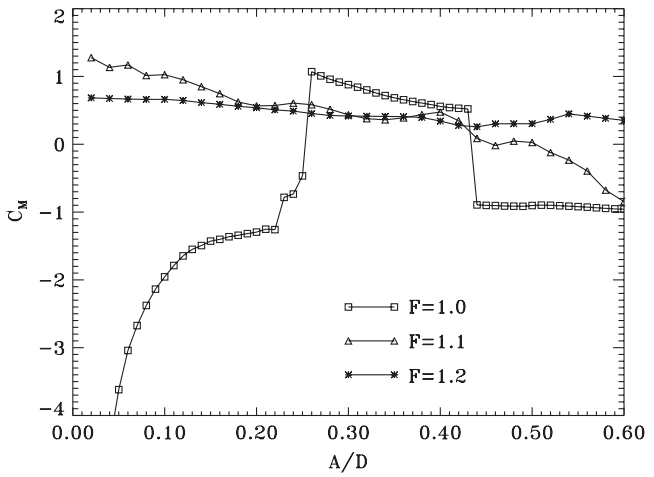

Fig. 17. Inertia force coefficient C_M, versus nondimensional excitation amplitude, for different values of reduced excitation frequency ($F \geqslant 1$).

3.1.3. Forcing at above the natural frequency

We finally consider forcing at above the resonant frequency. Two different cases are included, $f_e/f_s = 1.1$, and $f_e/f_s = 1.2$. Variation of C_{Lv}, C_M, C_{La}, $C_{L,\text{r.m.s.}}$, C_D, and $C_{D,\text{r.m.s.}}$ is shown in Figs. 16–21. The results of resonant forcing are also included for comparison. In both cases, the onset of lock-in, unlike the below resonant forcing, does not cause any discontinuities in the variation of the force coefficients. Also unlike the below resonant forcing, the variation of the force coefficients with A/D is complex and non-monotonic. The coefficient C_{Lv} exhibits the sharpest variations. All force coefficients however show discontinuities in their derivatives (easily identified in the plots), indicating that the flow passes through different flow states. The values of C_M are relatively close to the value of one for small amplitude oscillations, but deviate at higher values of A/D. The variation of the mean power dissipation in the flow with the reduced amplitude is shown in Fig. 22. In the above resonance forcing cases, there is a range of amplitude for which the flow settles to a less energetic state. This range seems to decrease with increasing F.

3.2. Visualization of the flow in the wake

We have made several visualizations of the flow in the wake behind the oscillating cylinder. We have included only the most representative visualizations. The criteria of selection are (a) the visualization corresponds to a combination of

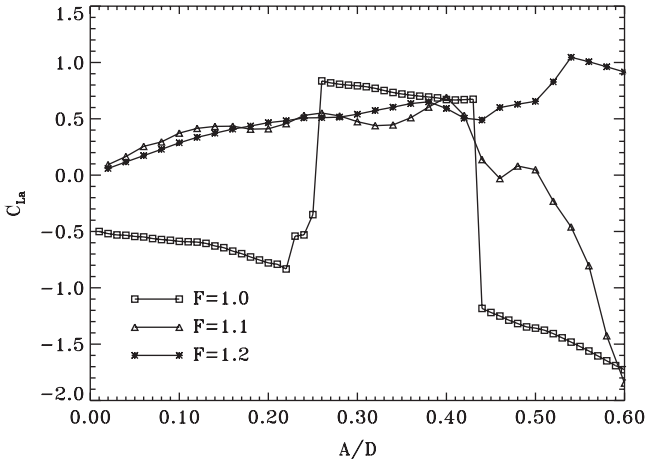

Fig. 18. Inertia force coefficient C_{La}, versus nondimensional excitation amplitude, for different values of reduced excitation frequency ($F \geqslant 1$).

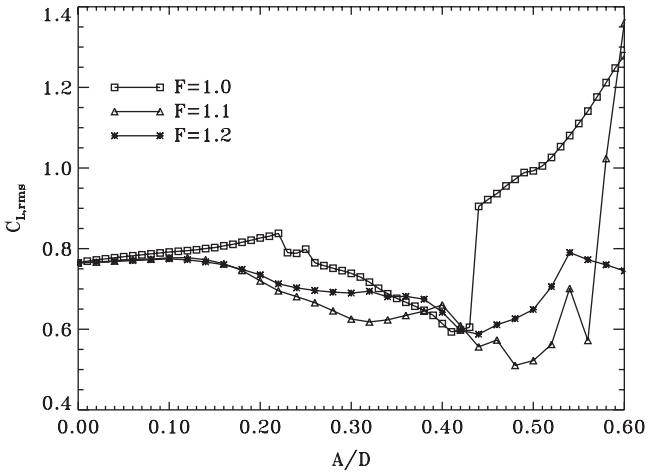

Fig. 19. R.m.s. fluctuation intensity of lift coefficient versus nondimensional excitation amplitude, for different values of reduced excitation frequency ($F \geqslant 1$).

frequency and amplitude related to a drastic change of the hydrodynamic force coefficients, or (b) the flow pattern in the wake changes drastically without some corresponding change of the hydrodynamic force coefficients. In all visualizations presented, the instantaneous displacement of the cylinder is equal to zero ($\eta/D = 0$). The flow visualizations demonstrate that variations of the forces on the cylinder are related to changes in the flow patterns in the wake, although it is also apparent that the relation is by no means straightforward. Things are further complicated by the fact that changes in the flow state in the wake, especially if they occur at a distance behind the cylinder, do not necessarily cause changes in the forces on the cylinder.

In this subsection, we will also make a comparison between what we observe here and the three basic patterns observed experimentally by Williamson and Roshko (1988), which we summarize here for easy reference: (a) a 2S type of vortex street, in which single vortices are formed on both sides of the cylinder, (b) an S + P type of vortex street, in which a single vortex is formed on one side of the cylinder, and a pair of vortices of opposite sign on the other side, and (c) a 2P type of vortex street, in which pairs of vortices of opposite sign are formed on both sides of the cylinder.

3.2.1. Resonant forcing

In Figs. 23(a)–(e) five different visualizations can be seen for the case of resonant forcing, which correspond to values of A/D equal to 0.14, 0.22, 0.35, 0.42 and 0.50, respectively. In Fig. 23(a) (snapshot for an A/D value before the first flow

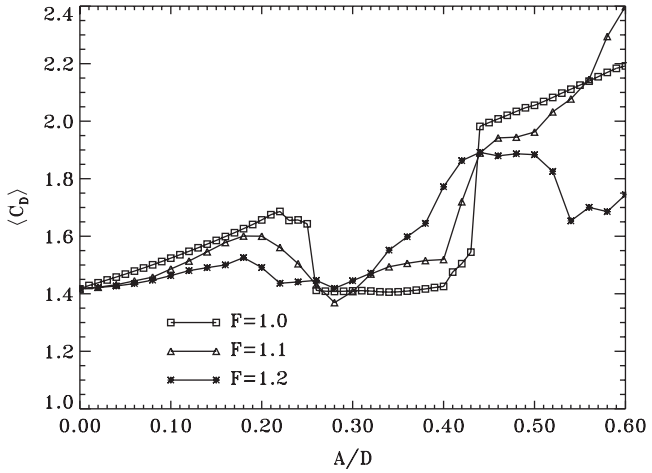

Fig. 20. Time-averaged drag coefficient versus nondimensional excitation amplitude, for different values of reduced excitation frequency ($F \geqslant 1$).

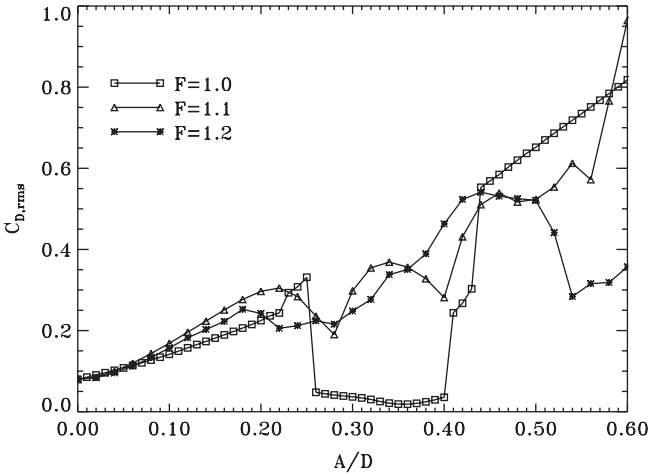

Fig. 21. R.m.s. fluctuation intensity of drag coefficient versus nondimensional excitation amplitude, for different values of reduced excitation frequency ($F \geqslant 1$).

bifurcation), we see a vortex street that starts as a 2S vortex street behind the cylinder. Farther downstream, vortices of the same sign merge forming vortices of larger area, and the wake widens. Fig. 23(b) shows a snapshot right before the first flow bifurcation. The vortex wake is qualitatively similar to the one seen in 23(a), with the important difference that the vortex merging occurs closer to the cylinder. Farther downstream, vortices of opposite sign are paired forming dipoles that move away from the center of the wake (in this case towards the upper side). Thus, the vortex street that started as 2S mode has turned into a single row of dipoles. This non-symmetric vortex street is characterized by a non-zero mean lift (time-averaged lift coefficient values of the order of 0.03).

Fig. 23(c), on the other hand, shows a snapshot after the first bifurcation, which is characterized by a "regular" 2S type vortex street. In consistency with the reduced mean drag, we observe a reduced width of the wake. Fig. 23(d) is a snapshot taken at the second bifurcation, and shows a wake in which the formation of dipoles starts almost immediately behind the cylinder. Unlike Figs. 23(a) and (b) however, dipoles are formed on both sides of the wake in an apparently random manner, indicative of a disordered vortex street.

Finally, Fig. 23(e), taken after the second bifurcation, shows yet another type of vortex wake, which could be described as a "partial S + P" mode, in the sense that on the one side of the wake (the upper in this instance) we see the appearance of vortex

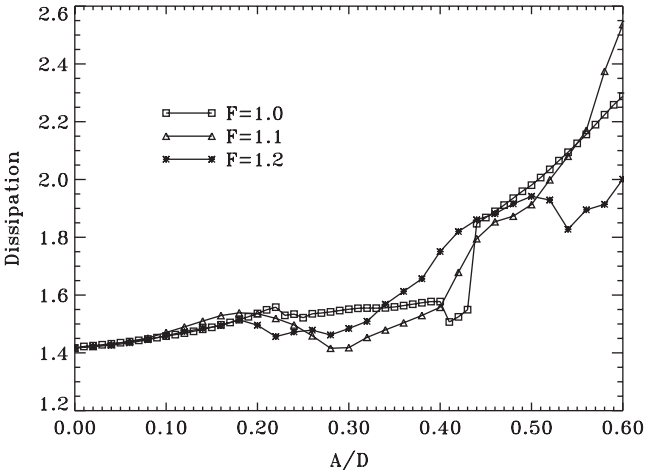

Fig. 22. Time-averaged nondimensional power dissipation versus nondimensional excitation amplitude, for different values of reduced excitation frequency ($F \geqslant 1$).

pairs, whereas on the other side (the lower) we see only single vortices. In reality, however, the pattern is much more complex and can be visualized best through animations of the results. Animations thus show that, at each cycle of vortex shedding, the vortex in the lower side splits into two vortices. The smaller vortex of the two is drawn to the upper side, whereas the larger remains in the lower side. The smaller vortex is accelerated by the induced velocity field of the larger vortices of opposite sign, and surpasses one by one the larger vortices. So, what appears in an instantaneous visualization as a "partial S + P" mode is in fact a "2S" mode modified by the vortex splitting process. Vortex splitting is therefore the mechanism by which these asymmetric vortex wakes are created. This type of vortex wake has not been reported before in the literature, as far as we know. In the rest of the paper we will refer to this mode of vortex shedding as a "partial S + P" for brevity.

Farther downstream, there is merging between single vortices of the same sign. Moreover, the positive vortices that were initially drawn into the upper part of the wake return in the far field to the lower side. The wake remains however non-symmetric with respect to the centerline. The asymmetric wake structure after the second bifurcation results again in non-zero mean lift (the time-averaged lift coefficient value is 0.133 for $A/D = 0.44$, increasing monotonically to 0.184 for $A/D = 0.60$).

3.2.2. *Forcing at below the natural frequency*

Figs. 24(a)–(d) show characteristic vortex streets behind a cylinder at below resonant forcing $f_e/f_s = 0.9$, for values of the parameter A/D equal to $0.05, 0.12, 0.30$ and 0.50, respectively. The first snapshot shows the vortex street for an amplitude of oscillation that is too low to cause lock-in. The vortex street starts as an orderly 2S type, which ends up disordered in the far wake. The snapshot in Fig. 24(b) shows the wake for an amplitude just over the threshold for lock-in. We observe a classical 2S type vortex street. The snapshots in Figs. 24(c) and (d) show wakes for lock-in states at higher amplitudes. In both figures, we see vortex streets of the 2S type. Downstream vortices of the same type conglomerate to form a two-shear-layer type of wake. Figs. 24(c) and (d) are remarkably similar; the only discernible difference is that, in the lock-in state at higher amplitude [Fig. 24(d)], the vortex street retains its 2S identity farther downstream than the one at lower amplitude [Fig. 24(c)]. Visualizations of the flow for $f_e/f_s = 0.8$ are presented in Figs. 25(a)–(d) for values of A/D equal to 0.06, 0.12 (both below the threshold for lock-in), 0.20 and 0.50 (above the threshold for lock-in). We can identify the same qualitative behavior as in Figs. 24(a)–(d).

3.2.3. *Forcing at above the natural frequency*

Figs. 26(a)–(f) show six representative flow visualizations for $f_e/f_s = 1.1$. The values of A/D at which the snapshots were taken are, respectively, $0.10, 0.20, 0.28, 0.40, 0.50$, and 0.56. We found it appropriate to include six visualizations because of the great variety of vortex configurations that we observed for oscillation frequencies above the natural frequency. Unlike the $f_e/f_s < 1$ cases, it is not easy to determine the onset of lock-in, because the flow for $f_e/f_s = 1.1$ is not periodic. We thus used the following definition for the onset of lock-in (Karniadakis and Triantafyllou, 1989): we consider that lock-in starts at the value of A/D at which the peak at f_e in the spectrum of the lift force becomes larger

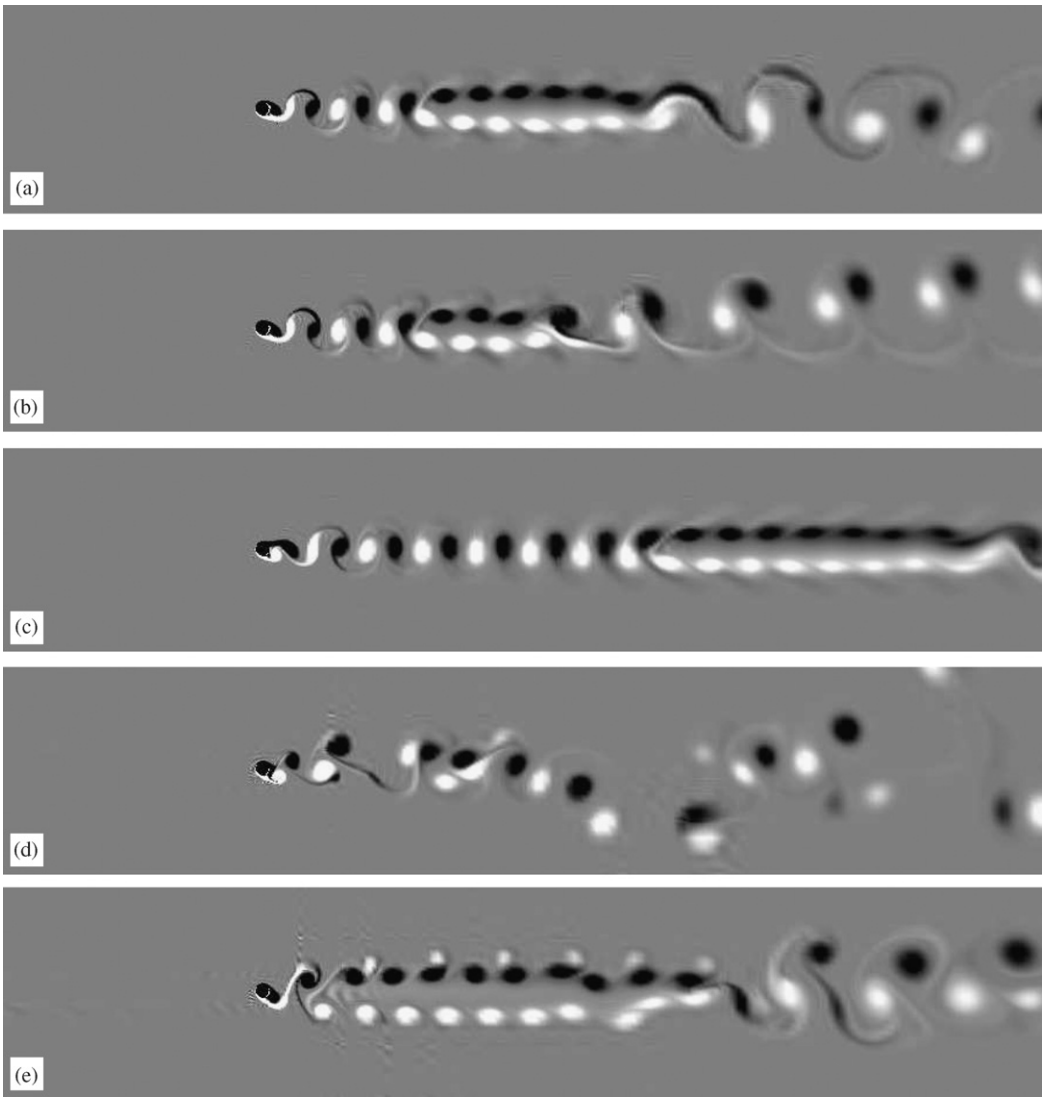

Fig. 23. Instantaneous vorticity isocontours, for different values of nondimensional excitation amplitude for $F = 1.0$: (a) $A/D = 0.14$, (b) $A/D = 0.22$, (c) $A/D = 0.35$, (d) $A/D = 0.42$, (e) $A/D = 0.50$.

than the peak at f_s. Based on this definition, the onset of lock-in for $f_e/f_s = 1.1$ was determined to occur for $A/D = 0.18$. In Fig. 26(a), which describes a non-lock-in state, we see a regular 2S vortex street behind the cylinder, which becomes considerably more complicated farther downstream. A similar structure, more complicated in the downstream region, is observed in Fig. 26(b), corresponding to a state slightly above lock-in (still quasi-periodic in time). The form of the vortex street is quite more complicated at higher A/D values [Figs. 26(c)–(e)], with pairs of vortices as well as single vortices being formed while the wake opens up. The observed disordered vortex streets cannot be classified as 2S, S+P nor 2P. Finally, for $A/D = 0.56$ [Fig. 24(f)], the vortex street becomes more ordered again, reminiscent of the double shear layer type of wake that we observed for forcing frequencies below the natural frequency.

In Figs. 27(a)–(f) we show six snapshots for $f_e/f_s = 1.2$. The values of A/D at which the snapshots were taken are, respectively, $0.10, 0.18, 0.26, 0.36, 0.46$, and 0.60. Figs. 27(a)–(f) follow the same trends as Figs. 26(a)–(f), with very unusual vortex patterns being observed. We have no explanation yet as to why are the flow states produced by forcing frequencies above the natural so more complicated than either the resonant or below resonant forcing.

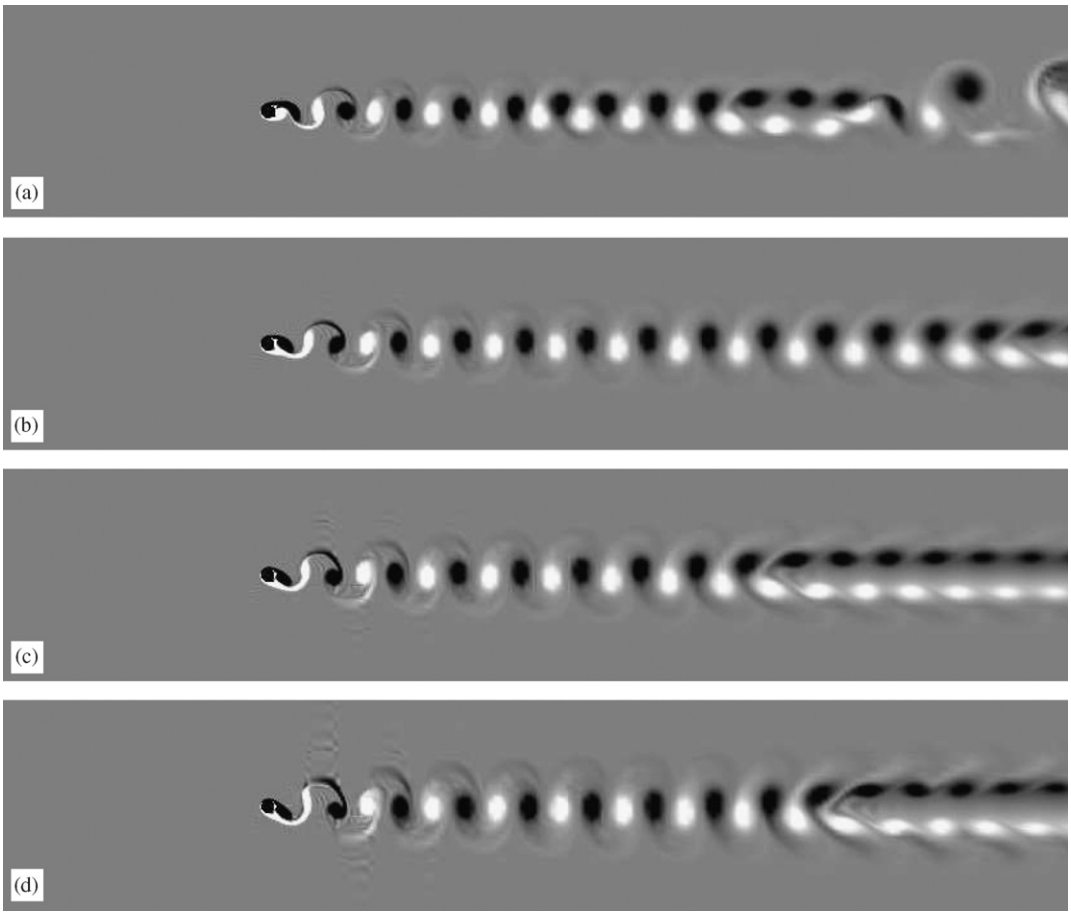

Fig. 24. Instantaneous vorticity isocontours, for different values of nondimensional excitation amplitude for $F = 0.9$: (a) $A/D = 0.05$, (b) $A/D = 0.12$, (c) $A/D = 0.30$, (d) $A/D = 0.50$.

4. Conclusions

We presented numerical results for the variation of the forces on an oscillating cylinder as a function of the amplitude-over-diameter-ratio, for several different frequencies of oscillation. The amplitude of oscillation was varied systematically from zero up to the value at which the excitation force becomes negative (i.e. the excitation becomes damping), because this is the maximum amplitude that can be observed in vortex-induced vibrations. Due to the low value of the Reynolds number of the simulation (400), this occurs when the amplitude becomes about half a diameter. At higher Reynolds numbers, typical of actual applications, the corresponding value of the amplitude is about one diameter, i.e. twice as much. Thus, the low Reynolds number (and two-dimensionality) of the simulation prohibits direct application of our results for the prediction of vortex-induced vibrations of real structures. We believe, however, that our conclusions are of interest in the development of models for the forces on real structures.

Three different cases have been considered, oscillation of the cylinder at the natural frequency of vortex shedding for a stationary cylinder (resonant forcing), oscillation at a frequency below the natural frequency (below resonance forcing), and oscillation at a frequency above the natural frequency (above resonance forcing). Two frequencies below and two frequencies above resonance have been considered. We observed that the dynamics of the flow is very different below resonance and above resonance. This has also been reported in the numerical simulations of Anagnostopoulos (2000), at low Reynolds numbers, and in the experiments of Carberry et al. (2005), at much higher Reynolds numbers.

In our simulations, there are two main qualitative differences between the results for below resonance, and those for resonant and above resonance forcing, not reported before. The first difference is that, below resonance, there is a smooth variation of the hydrodynamic coefficients with the amplitude-to-diameter-ratio A/D. The only discontinuity is in the slope of the coefficients, observed at the value of A/D for which lock-in starts (this gives an easy way to

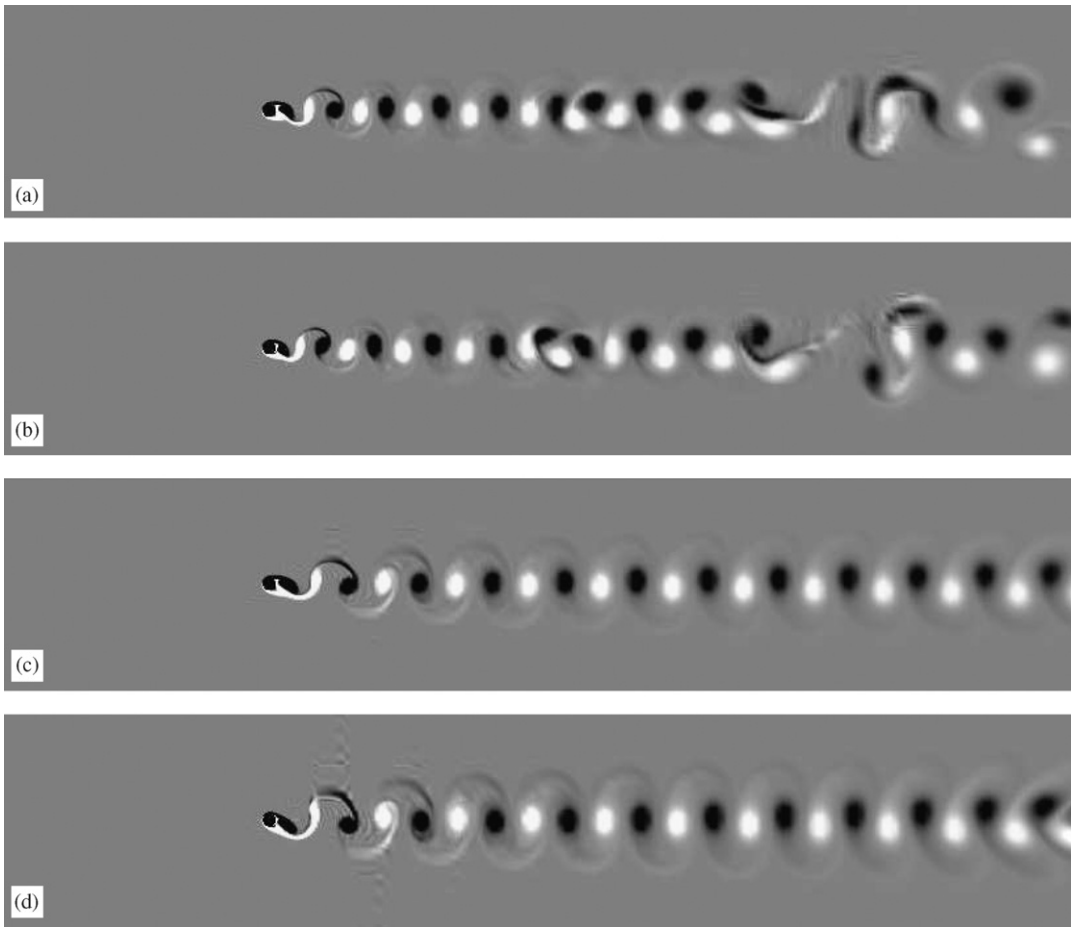

Fig. 25. Instantaneous vorticity isocontours, for different values of nondimensional excitation amplitude for $F = 0.8$: (a) $A/D = 0.06$, (b) $A/D = 0.12$, (c) $A/D = 0.20$, (d) $A/D = 0.50$.

unambiguously determine the onset of lock-in). For resonant and above resonance forcing, on the other hand, there are several discontinuities in the variation of the hydrodynamic force coefficients with A/D, not related to the onset of lock-in. The onset of lock-in in fact has no easily visible effect on the forces. The resonant forcing seems unique (or singular) in that humps are observed in all hydrodynamic coefficients, at the same values of A/D. Above resonance, changes of the hydrodynamic coefficients appear in a sharp but continuous manner, whereas the derivatives of the hydrodynamic coefficients are discontinuous.

The second important difference is that, below resonance, we only observed 2S modes of vortex shedding, which, once lock-in occurs, correspond to time-periodic and spatially ordered vortex streets. Above resonance, on the other hand, other non-periodic in time and spatially disordered vortex streets are present. A "partial S + P" mode has been observed for resonant forcing at high amplitude. We termed this "partial", in the sense that the wake starts with two single vortices, however one of them splits into two, and the small vortex originating from the splitting enters the other side of the wake. Two sharp transitions occur for resonant forcing. After the first one, at $A/D = 0.26$, the average drag coefficient drops slightly below that of the stationary cylinder. The second transition (from a 2S mode to the more complex "partial S + P" pattern) is accompanied by an increase of the width of the wake and of the average drag coefficient. In many cases, the emergence of complicated vortex patterns at a distance downstream from the cylinder was not associated with any consistently observed change of the hydrodynamic force coefficients.

Regarding the scaling of the forces acting on the cylinder, we note that, using the concept of an inertia force for the component of the lift force that is 180 degrees out of phase with the acceleration does not seem physically justified. This is based on the observation that the "added mass" coefficient C_M has positive values close to unity only for resonant and above resonance forcing, and only for a certain range of values of A/D. We conclude therefore that scaling both

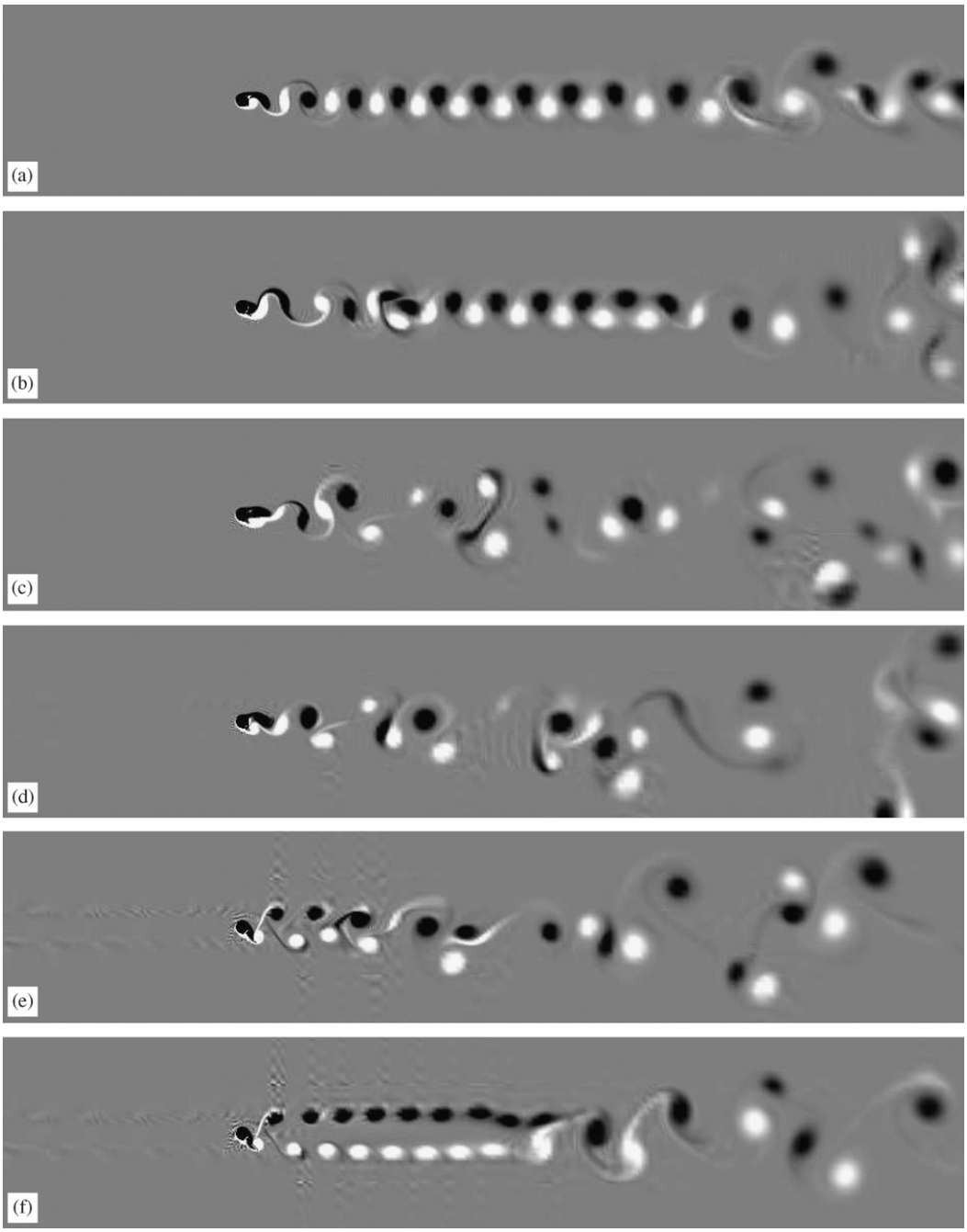

Fig. 26. Instantaneous vorticity isocontours, for different values of nondimensional excitation amplitude for $F = 1.1$: (a) $A/D = 0.10$, (b) $A/D = 0.20$, (c) $A/D = 0.28$, (d) $A/D = 0.40$, (e) $A/D = 0.50$, (f) $A/D = 0.56$.

components of the lift force with the dynamic pressure, in other words using coefficients C_{Lv} and C_{La}, in lieu of C_{Lv} and C_M, is overall preferable. This conclusion is in agreement with earlier work by Sarpkaya [see Sarpkaya (2004), for a summary], and we believe that it carries through to higher Reynolds numbers as well.

Comparing our results to the experiments of Williamson and Roshko (1988), which are at almost the same Reynolds number, we observe the following: first the value of the Strouhal number in our simulation of the flow past the stationary cylinder is about 10% higher than the experimental one, as is to be expected since our simulation is

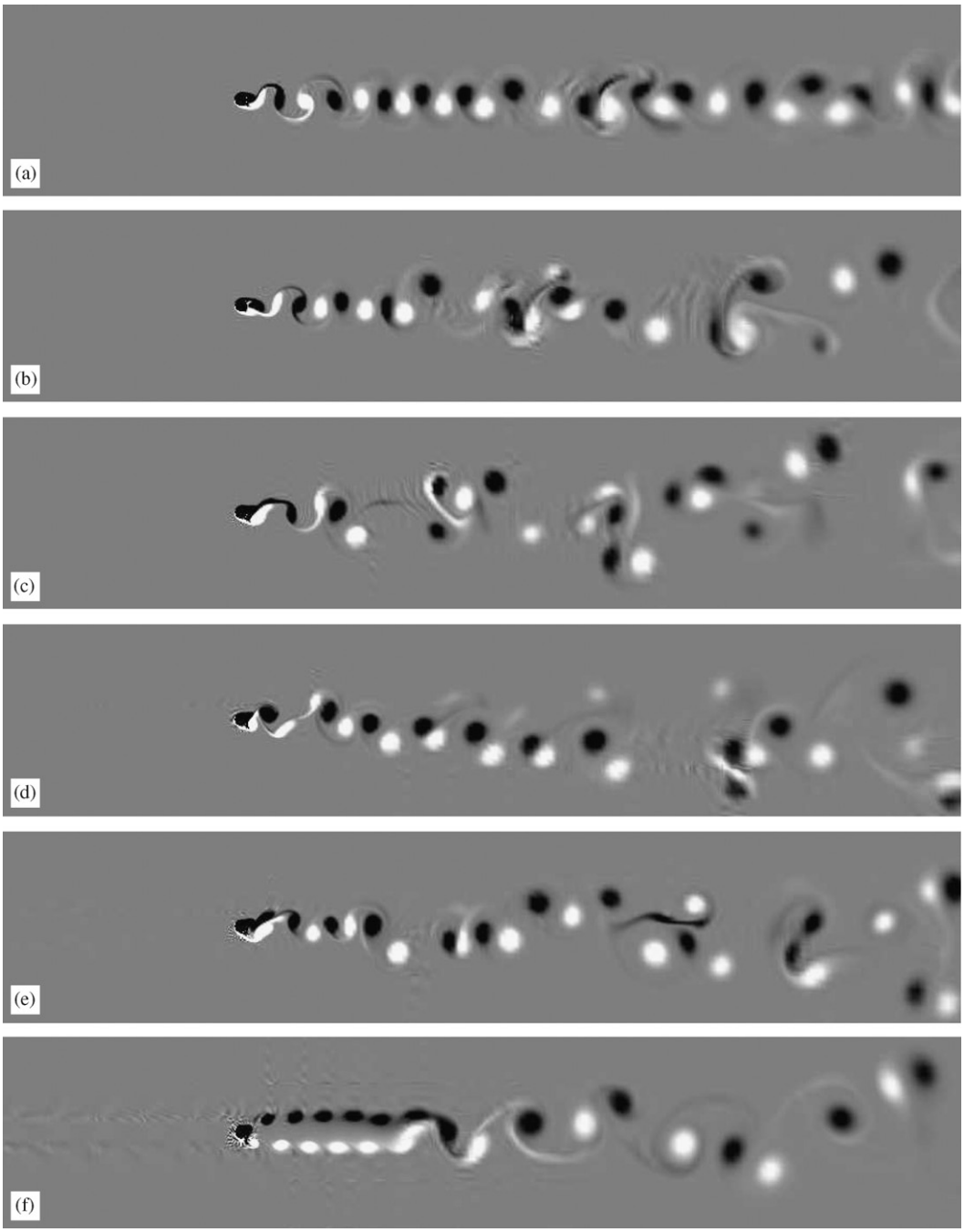

Fig. 27. Instantaneous vorticity isocontours, for different values of nondimensional excitation amplitude for $F = 1.2$: (a) $A/D = 0.10$, (b) $A/D = 0.18$, (c) $A/D = 0.26$, (d) $A/D = 0.36$, (e) $A/D = 0.46$, (f) $A/D = 0.60$.

two-dimensional. Our parameter $F = f_e/f_s$ has been based on the computed Strouhal number. The question then is how do the two-dimensional simulation results compare with the experimental ones for the same values of the frequency ratio F. Our results agree with the experiments in that we also observed the 2S mode for resonant forcing. There is no mention in Williamson and Roshko (1988), however, of any of the complex flow patterns and transitions that we observed for $F = 1$ and $F > 1$, at least not for the amplitudes of oscillation that we considered. (They have reported more complex patterns at higher amplitudes.) It is not clear as yet whether this difference is due to the

two-dimensionality of our simulations. One way to settle this issue would be by performing three-dimensional simulations for the same values of the reduced frequency and amplitude of oscillations that we observed the complex vortex patterns, and compare the outcome. Finally, as far as vortex dynamics is concerned, our main finding is the formation of the asymmetric "partial S + P" mode, which results from a vortex splitting instability. It is worth investigating whether this mode is also present in three dimensions.

Appendix A. Resolution tests

Our resolution tests were performed for the case of resonant forcing ($f_e = f_s$), for $A/D = 0.50$. As the flow gradients are in general sharper at higher oscillation amplitudes, we believe that the adequacy of discretization is also justified for the lower amplitude values of the present study.

First, we performed temporal resolution tests. Here, we have used the standard spatial discretization, consisting of 464 macro-elements, with 9×9 elemental resolution. Four values of the numerical time step were tested, namely $\Delta t = 0.00075$, 0.0015, 0.00225, and 0.0030. The computed force coefficient values are reported in Table 1. The numbers show that the deviations between the highest resolution results ($\Delta t = 0.00075$) and all others are in most cases in the third decimal point. This suggests that the values of Δt that we have used throughout the paper ($\Delta t \leqslant 0.0015$) correspond to practically negligible temporal discretization errors.

Next, we performed spatial resolution tests, corresponding to p-type of mesh refinement. Here, $\Delta t = 0.0015$. We have maintained the standard spectral element skeleton (464 macro-elements), and used different polynomial degrees, corresponding to 7×7, 9×9, and 11×11 elemental resolution. The computed values of the force coefficients are reported in Table 2. Again, the results show negligible differences between the highest resolution (11×11) and the other two. This illustrates the adequacy of the spatial resolution (464 macro-elements with 9×9 elemental resolution) used throughout the paper.

Table 1
Temporal resolution tests, for $F = 1.0$, $A/D = 0.50$: computed values of force coefficients, for different values of the numerical time step

Δt	C_{lv}	C_M	C_{la}	C_D	$C_{D,\text{r.m.s.}}$	C_L	$C_{L,\text{r.m.s.}}$
0.000750	0.2183846	−0.9066322	−1.362657	2.05414	0.651524	0.165215	0.996396
0.001500	0.2161986	−0.9035547	−1.358031	2.05535	0.651788	0.166407	0.993117
0.002250	0.2141826	−0.9000216	−1.352721	2.05595	0.651869	0.167618	0.989255
0.003000	0.2119567	−0.8976544	−1.349163	2.05734	0.651926	0.169330	0.986695

Table 2
Spatial resolution tests, for $F = 1.0$, $A/D = 0.50$: computed values of force coefficients, for different values of elemental resolution

Resolution	C_{lv}	C_M	C_{la}	C_D	$C_{D,\text{r.m.s.}}$	C_L	$C_{L,\text{r.m.s.}}$
7×7	0.2102251	−0.8868189	−1.332878	2.05550	0.650862	0.161505	0.978883
9×9	0.2161986	−0.9035547	−1.358031	2.05535	0.651788	0.166407	0.993117
11×11	0.2193779	−0.9227460	−1.386876	2.06052	0.648169	0.167330	1.012410

References

Anagnostopoulos, P., 2000. Numerical study of the flow past a cylinder excited transversely to the incident stream. Part 1: Lock-in zone, hydrodynamic forces and wake geometry. Journal of Fluids and Structures 14 (6), 819–851.

Baek, S.J., Lee, S.B., Sung, H.J., 2001. Response of a circular cylinder wake to superharmonic excitation. Journal of Fluid Mechanics 442, 67–88.

Bearman, P.W., 1984. Vortex shedding from oscillating objects. Annual Review of Fluid Mechanics 16, 195–222.

Blackburn, H.M., Henderson, R.D., 1999. A study of two-dimensional flow past an oscillating cylinder. Journal of Fluid Mechanics 385, 255–286.

Blackburn, H.M., Govardhan, R.N., Williamson, C.H.K., 2001. A complementary numerical and physical investigation of vortex-induced vibration. Journal of Fluids and Structures 15 (3–4), 481–488.

Carberry, J., Sheridan, J., Rockwell, D., 2005. Controlled oscillations of a cylinder: forces and wake modes. Journal of Fluid Mechanics 538, 31–69.

Delaunay, Y., Kaiktsis, L., 2001. Control of circular cylinder wakes using base mass transpiration. Physics of Fluids 13 (11), 3285–3302.

Evangelinos, C., Karniadakis, G.E., 1999. Dynamics and flow structures in the turbulent wake of rigid and flexible cylinders subject to vortex-induced vibrations. Journal of Fluid Mechanics 400, 91–124.

Gopalkrishnan, R., 1993. Vortex-induced forces on oscillating bluff cylinders. Ph.D. Thesis, MIT, Cambridge, MA.

Guilmineau, E., Queutey, P., 2002. A numerical simulation of vortex shedding from an oscillating circular cylinder. Journal of Fluids and Structures 16, 773–794.

Kaiktsis, L., Monkewitz, P.A., 2003. Global destabilization of flow over a backward-facing step. Physics of Fluids 15 (12), 3647–3685.

Karniadakis, G.E., 1989. Spectral element simulations of laminar and turbulent flows in complex geometries. Applied Numerical Mathematics 6, 85–105.

Karniadakis, G.E., Triantafyllou, G.S., 1989. Frequency selection and asymptotic states in laminar wakes. Journal of Fluid Mechanics 199, 441–469.

Karniadakis, G.E., Israeli, M., Orszag, S.A., 1991. High-order splitting methods for the incompressible Navier–Stokes equations. Journal of Computational Physics 97, 414–443.

Sarpkaya, T., 2004. A critical review of the intrinsic nature of vortex-induced vibrations. Journal of Fluids and Structures 19, 389–447.

Williamson, C.H.K., Govardhan, R., 2004. Vortex-induced vibrations. Annual Review of Fluid Mechanics 36, 413–455.

Williamson, C.H.K., Roshko, A., 1988. Vortex formation in the wake of an oscillating cylinder. Journal of Fluids and Structures 2, 355–381.